An Efficient Self-supporting Infill Structure for Computational Fabrication

Shengfa Wang[1]   Zheng Liu[1]   Jiangbei Hu[† 1,3] (ID)   Na Lei [1]   Zhongxuan Luo [2]

[1]International School of Information Science&Engineering, Dalian University of Technology
[2]School of Software Technology, Dalian University of Technology
[3]School of Computer Science and Engineering, Nanyang Technological University

Abstract

Efficiently optimizing the internal structure of 3D printing models is a critical focus in the field of industrial manufacturing, particularly when designing self-supporting structures that offer high stiffness and lightweight characteristics. To tackle this challenge, this research introduces a novel approach featuring a self-supporting polyhedral structure and an efficient optimization algorithm. Specifically, the internal space of the model is filled with a combination of self-supporting octahedrons and tetrahedrons, strategically arranged to maximize structural integrity. Our algorithm optimizes the wall thickness of the polyhedron elements to satisfy specific stiffness requirements, while ensuring efficient alignment of the filled structures in finite element calculations. Our approach results in a considerable decrease in optimization time. The optimization process is stable, converges rapidly, and consistently delivers effective results. Through a series of experiments, we have demonstrated the effectiveness and efficiency of our method in achieving the desired design objectives.

CCS Concepts

*• **Computing methodologies** → **Modeling and simulation; Model development and analysis;** • **Applied computing** → Computer-aided design;***

1. Introduction

Additive manufacturing technology offers a distinct advantage over traditional subtractive manufacturing by enabling the creation of intricate internal structures. Consequently, optimizing the design of these internal structures has emerged as a significant focus within the field. Several structures have been proposed [PP19], including the Skin-frame structure [WWY*13], the Honeycomb-cell structure [LSZ*14], the Media-axis structure [ZXW*15], the Polyhedral Voronoi [MHSL18], and Crossfill [KWW19]. These methods aim to achieve lightweight and high-stiffness outcomes. However, it is important to note that some of these solutions overlook the printability of the internal structure. Hence, algorithm designers must also consider the inclusion of supporting structures to ensure successful fabrication.

Although 3D printing software is capable of detecting and adding support structures to ensure printability, it is important to address the issue of closed cavity structures that may cause the internal support structure to remain after printing. This can have a detrimental impact on the model and hinder the optimization process. To tackle this challenge, experts have proposed various solutions, including Rhombic [WWZW16], Support-free hollowing [WQL*17], Elliptic hollowing [LFR*18] and Periodically hollowing [XLY*21]. The underlying concept of these methods is to ensure the self-supporting nature of each cavity to enable successful printing. However, it is worth noting that most of these methods require a high-quality finite element mesh during the optimization phase to avoid jaggedness. This requirement poses a significant computational burden, making the optimization process more complex and time-consuming.

We have created a new approach to address the difficulties previously mentioned, which involves optimizing the internal structure. Our approach focuses on ensuring self-supporting characteristics within the model while addressing the computational cost associated with stiffness optimization. As depicted in Fig. 1, we initiate the process with an initial model and discretize its internal space using regular polyhedron elements. Through iterative optimization of the wall thickness of these elements, marked in yellow regions, we generate self-supporting cavities. This iterative optimization allows us to substantially reduce the optimization time. By utilizing self-supporting polyhedron elements that align with the elements in finite element calculations, we avoid jaggedness and enable faster computations. Next, we optimize the topology of the structure by merging redundant elements based on the results of the thickness optimization. The final optimized structure demonstrates improved

---

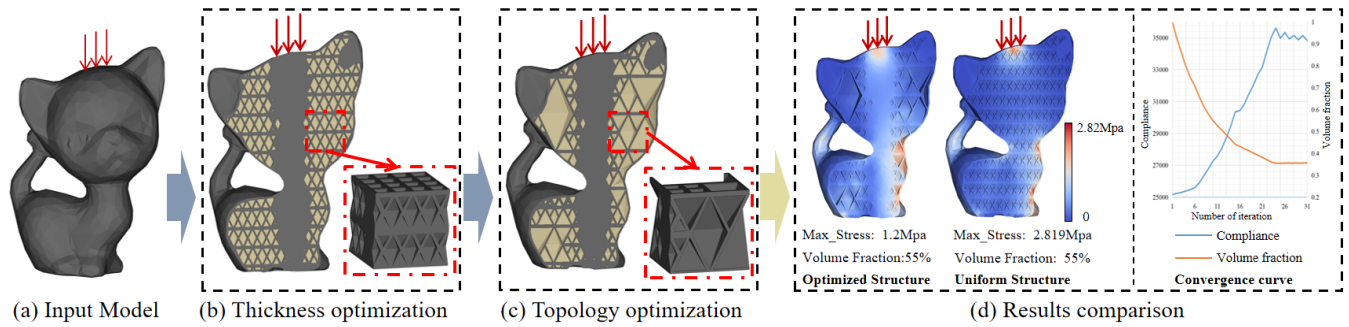† Corresponding author. Email: hjb941220@dlut.edu.cn

Figure 1: *Illustration of the optimization process. (a) Input model. (b) The thickness optimization. (c) The topology optimization. (d) Comparison of stiffness results between the optimized structure and a uniformly filled structure, and the convergence curve of compliance and volume fraction during optimization.*

stiffness compared to a uniformly infilled structure. Overall, our method effectively achieves self-supporting characteristics within the model and significantly reduces computational costs. Additionally, the optimized structure exhibits enhanced stiffness properties compared to those of traditional uniformly filled structures.

The main contributions of our approach can be summarized as follows:

- Utilization of a Self-Supporting Octahedral-Tetrahedral Structure: We employ a self-supporting octahedral-tetrahedral structure to fill the model. This choice facilitates efficient generation and fusion of the elements, resulting in a structure that is compatible with fast finite element calculations.
- Efficient Optimization Strategy for Finite Element Analysis: We propose an efficient optimization strategy for the finite element analysis of the structure. This strategy includes both thickness optimization and topology optimization, ensuring the overall optimization process is effective and time-efficient.

By combining these contributions, our approach enables the creation of optimized structures with improved performance and reduced computational costs.

2. Related Work

In recent years, the field of 3D printing has witnessed the emergence of numerous methods that cater to diverse geometric and structural requirements. Our study focuses specifically on three key areas of research: lightweight infill structures, self-supporting structures, and structure optimization [LSWW14, GZR*15]. These areas are of particular relevance to our investigation and will serve as the primary areas of focus for our research.

2.1. Lightweight infill structures

Several optimization methods have been proposed for designing the internal structure of 3D models, taking into consideration various requirements such as stiffness [SVB*12], stability, printability, and material usage efficiency. Wang et al. [WWY*13] introduced a sparse optimization approach that generates a skin-frame structure, considering multiple constraints in 3D models. Zhang

et al. [ZXW*15] utilized the medial axis as an alternative to the frame structure, enabling effective transfer of external loads to the inner core structure. Lu et al. [LSZ*14] and Sá et al. [SM-REC15] employed honeycomb-cell structures, which strike a balance between material utilization and stiffness performance. Inspired by nature, porous structures have also been explored for their lightweight and strong structural properties. Wu et al. [WAWS18] proposed a method for generating bone-like porous structures using topology optimization. Martínez et al. [MHSL18] and Kuipers et al. [KWW19] presented microstructures designed to achieve specific elastic properties. In addition, Hu et al. [HWL*20] employed Triply Periodic Minimal Surface (TPMS) to generate lightweight structures with high stiffness by efficiently controlling the function. Similarly, Zhang et al. [ZWL*22] controlled the function to create cavities, allowing for a reduction in weight while maintaining stiffness. However, the structures proposed in [WWY*13, LSZ*14, ZXW*15, ZWL*22, SMREC15, WAWS18] are not self-supporting. Consequently, additional support structures may be required during the printing process, leading to difficulties in their removal.

2.2. Self-supporting structures

To eliminate the need for additional support structures during printing, the development of self-supporting structures for filling the interior of models has been explored in various studies [LGC*18, BAH11, ZZW*21, VGB14a]. Luo et al. [LBRM12] proposed the Chopper framework which breaks down a large 3D object into smaller parts that can be printed. J. Vanek et al. [VGB*14b] also follows a comparable strategy (PackMerger) for decomposition. In the case of PackMerger, it divides 3D objects into various shell components and then optimizes the process to minimize the requirement for support materials and printing duration. Gaynor et al. [GG16] achieved self-supporting printing by applying a series of projection operations that enforce minimum length scale requirements. Similar approaches were also employed by Zhou et al. [ZSZ21] and Luo et al. [LSLL20] to address self-supporting printing. Leary et al. [LMT*14] proposed a post-processing method that evaluates manufacturing time and component mass to ensure self-supportability by identifying feasible orientations. Reiner and Lefebvre. [RL16] developed an interactive modeling tool for designing self-supporting models. Wu et al. [WWZW16] introduced

the rhombic structure, which is adaptively refined based on physical properties such as the center of mass and stress distribution. Wang et al. [WLW*18] generated sparser structures through hollowing. They also proposed a sparsity optimization framework with overhanging constraints for generating support-free frame structures [WQL*17]. Yang et al. [YCF18] presented a simple hollow-to-fill algorithm for generating support-free inner surfaces using shape optimization. Xie and Chen [XC17] proposed a polyhedron element-based approach for creating support-free interior cavities. Lee et al. [LFR*18] introduced a support-free elliptic hollowing method. Bi et al. [BTX20] derived a self-supporting topology optimization method based on BESO [HX08] that controls the support relationship between elements in the upper and lower layers. However, many of these self-supporting structures require high-quality finite elements in the calculations to avoid jaggedness, resulting in significant computational costs.

2.3. Structure optimization

Structure optimization aims to control the material distribution within a design domain to achieve desired physical properties. Since the introduction of topology optimization (TO) in the 1980s [BK88], various TO methods have been successfully employed in many fields for structure optimization [ZZG16]. These methods include the homogenization method [BK88, SK91], solid isotropic material with penalization (SIMP) [Ben89, Roz01, ZR91], level set method [SW00, WWmG03], evolutionary structural optimization (ESO) [XS93], Bi-directional ESO [HX08], moving morphable component (MMC) method [GZZ14], and moving morphable void (MMV) [ZYZ*17]. A comprehensive overview of these methods can be found in [SM13, ZNLC14]. With the advancement of 3D printing technologies [PAHA18, WM17, TKF15], there is an increasing demand for efficient structure optimization methods that can generate more complex structures with superior physical properties.

3. Self-Supporting Polyhedral Structure for Fast Calculation

The infilling structure of the model is composed of a periodic mixed structure consisting of octahedra and tetrahedra. This unique structure meets the self-supporting requirements while also facilitating regular rearrangement and division. It proves advantageous in both the construction and optimization of the overall structure. Furthermore, the integration of this structure with the finite element method allows for algorithmic adjustments that enable faster calculations, greatly enhancing optimization efficiency.

3.1. Polyhedron elements

Our approach utilizes regular octahedrons and tetrahedrons as periodic polyhedron elements. Each of these polyhedrons can be further subdivided into smaller, similar octahedrons and tetrahedrons, as shown in Fig. 2. This characteristic proves advantageous for both the initialization and optimization of the structures. Specifically, we employ a large octahedron that encompasses the entire model as an initial structure. Then, we proceed to fill the model's interior with regular polyhedron elements using the aforementioned method. By employing this approach, we only need to calculate
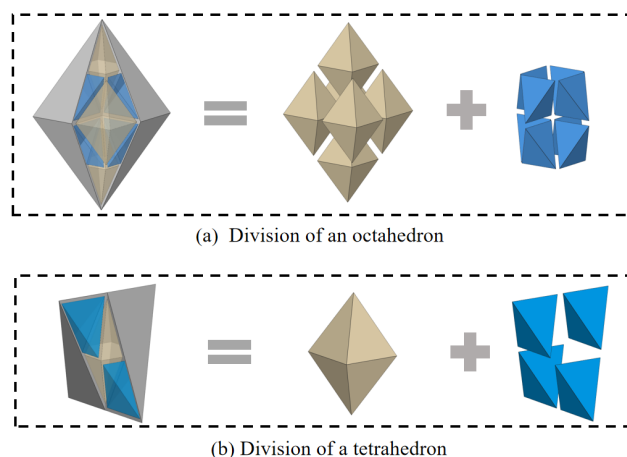
(a) Division of an octahedron

(b) Division of a tetrahedron

Figure 2: *Illustration of the octahedron and tetrahedron division. (a) A regular octahedron can be divided into six identical small octahedrons and eight identical small tetrahedrons. (b) A regular tetrahedron can be divided into one small octahedron and four identical small tetrahedrons.*

the volume fraction of each individual polyhedron element during the optimization process. Subsequently, we can generate self-supporting cavities within the polyhedron elements, facilitating the overall structure optimization of the model.

3.2. Self-supporting structure

The self-supporting capability of the structure refers to its ability to support itself, including both the polyhedral elements and the model shell. In order to simplify the analysis, we will primarily concentrate on the octahedron, as it shares similarities with the tetrahedron.

The self-supporting nature of a polyhedral element depends on the alignment between the normal direction of its inner surface and the printing direction. Illustrated in Figure 3, for a face with a normal vector n_{Face} and a unit vector representing the printing direction n_{Print}, the following condition must be satisfied

$$\arccos \frac{n_{Face} \cdot n_{Print}}{\mid n_{Face} \mid \mid n_{Print} \mid} \leq \frac{\pi}{2} + \alpha, \qquad (1)$$

where α is the maximum angle of overhang allowed by the 3D printer, and is set to $\alpha = \frac{\pi}{4}$ by default. The self-supporting can also be controlled directly by the shape parameters of the polyhedron:

$$\frac{h}{w} \geq \tan \alpha, \qquad (2)$$

where h and w are two axial lengths of the outer surface of a octahedron, respectively.

In cases where certain sections of the model shell lack self-supporting properties, internal support is necessary. The process involves examining all the polyhedron elements and determining if any of them intersect with the triangles comprising the outer surface of the model. If a triangular facet is identified as non-self-supporting, the internal cavity of the corresponding polyhedron element needs to be adjusted to provide the required support.

Taking advantage of the viscosity of the 3D printing material during extrusion, we can ensure that a short suspended length does not result in material collapse. Utilizing this principle, we regulate the cavity size of the polyhedral elements that intersect with non-self-supporting shells. In Fig. 3, the axial length w of the polyhedral element and the horizontal wall thickness t of a cavity are determined based on the maximum unsupported length ε_{max}. If the calculated ε is smaller than the maximum unsupported length permitted by the printer, it indicates self-supporting capability and can be expressed as follows:

$$\varepsilon = \sqrt{2}(2w - 2t) < \varepsilon_{max}. \tag{3}$$

It is clear that, given the size of the polyhedron element w and the maximum unsupported length ε_{max}, the minimum volume rate of the polyhedron element can be obtained:

$$x_{min} = \frac{V_{min}}{V_p} = 1 - \left(\frac{w - t_{min}}{w}\right)^3 = 1 - \left(\frac{\sqrt{2}\varepsilon_{max}}{4w}\right)^3, \tag{4}$$

where V_p represents the volume of the polyhedron element, and V_{min} represents the smallest volume by removing a cavity inside the polyhedron element. Therefore, by partitioning the polyhedron elements at the boundaries, we ensure that the outer shell can be printed without the need for any support structures.

The self-supporting structure most akin to ours is the one created by Wu et al. [WWZW16]. Nevertheless, their design employs 2D shapes extruded into 3D infills. This approach comes with constraints on design adaptability and boundary cohesion, which curtails its capacity for achieving lightweight structures. In contradistinction, our designed structures are fundamentally self-supporting in three dimensions. Illustrated in Figure 2, our methodology permits smooth subdivision or fusion of elements, enabling us to enhance strength and decrease volume.

3.3. Polyhedral structure for fast calculation

In order to accurately analyze and calculate the structure and its thickness, the finite element method is employed, which typically involves multiple iterations and can be computationally demanding. However, leveraging the unique geometric properties of the polyhedron element structure allows for a reduction in computational burden.

By coupling the structure with hexahedral finite elements, the local intricate structure can be simplified into a local equivalent material density. This simplification facilitates the determination of the volume fraction for each polyhedral element and the equivalent material density for each finite element. This approach not only accelerates the computation process, but also eliminates jaggedness, resulting in reduced hardware requirements and optimization time. For further information on the calculation methodology, please refer to Section 4 of this study.

4. Modeling and optimization

4.1. Stiffness problem modeling

The objective of our approach is to generate self-supporting interior structures while maximizing stiffness. In classical structural
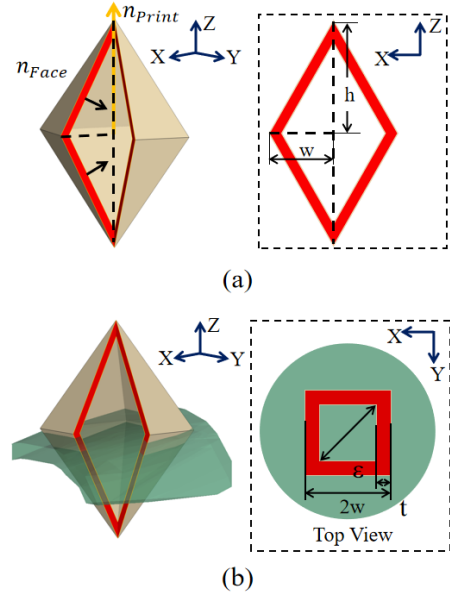

Figure 3: *Illustration of the self-supporting of the cavities and the shell. (a) Self-supporting polyhedron element with a cavity (yellow) and a cross-section (red). The black arrow represents the normal direction of the inner surface and the yellow arrow represents the printing direction. (b) Self-supporting of the shell (green) and the cross-section.*

optimization problems, the optimization objective is typically defined in terms of structural compliance. The optimization problem can be formulated as follows:

$$\min \quad C = \frac{1}{2}\mathbf{u}^T\mathbf{K}\mathbf{u}, \tag{5}$$

s.t.

$$\sum_{k=1}^{N} v_k x_k < V_{target}, \tag{6}$$

$$x_k = \begin{cases} x_{min}, & \text{for void element,} \\ 1, & \text{for solid element,} \end{cases} \tag{7}$$

where C is the overall compliance, $\mathbf{u}$ is the displacement matrix, $\mathbf{K}$ is the overall stiffness matrix, V_{target} is the target volume, v_k is the volume of the i-th hexahedral element, and x_k is the state of the k-th hexahedral element.

In this approach, since we fill the interior of the model with polyhedron elements, the aforementioned expression can be reformulated as follows:

$$\min \quad C = \sum_{i=1}^{n_e} C_i = \sum_{j=1}^{n} u_{ij}^T K_{ij} u_{ij}, \tag{8}$$

$$\frac{V_{solid}}{V_{voxel}} = \qquad 1 \qquad \frac{n-1}{n} \qquad \frac{n-2}{n} \qquad \bullet\bullet\bullet \qquad \frac{2}{n} \qquad \frac{1}{n} \qquad 0$$
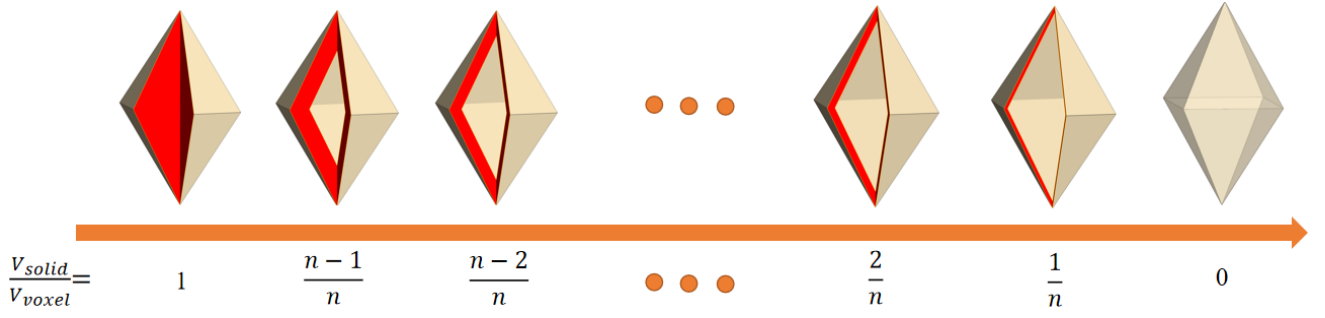
Figure 4: *Volume evolution of octahedral polyhedron elements. From left to right, the octahedral polyhedron elements have a gradual change in its volume from solid to empty. The process is divided into 6 levels, and the volume change between each adjacent stage is constant at 0.2.*

s.t.

$$V_{target} = \sum_{i=1}^{N} v_i x_i, \qquad (9)$$

$$x_i = \begin{cases} x_{min}, & \text{for void element,} \\ 1, & \text{for solid element,} \end{cases} \qquad (10)$$

where the total compliance C is represented by the sum of the compliance of n_e polyhedron elements, K_{ij} represents the element stiffness matrix of the j-th hexahedral element that composes the i-th polyhedron element, and u_{ij} represents the displacement of the corresponding element.

The cavity within the polyhedron elements is regulated by adjusting the wall thickness, which is equivalent to modifying the volume fraction of each element. By adopting this approach, the optimization emphasis shifts from individual hexahedral units to the polyhedron elements residing within the model. This enables the implementation of efficient and well-founded design schemes through subsequent algorithmic optimization processes.

4.2. Wall-thickness optimization

The wall thickness of the polyhedral elements is a critical factor influencing both the volume and structural stiffness of the model. Hence, our optimization approach places significant emphasis on optimizing the wall thickness. Subsequently, the topology of the structure is adjusted based on the optimized wall thicknesses. To ensure the rationality of the optimization process, we adopt a direct method that involves iteratively optimizing the volume fraction of the polyhedral elements. This optimization is carried out in conjunction with finite element analysis, enabling iterative refinement of the volume fraction to meet the desired design objectives.

To accelerate the calculations, we initially discretize the wall thicknesses of octahedron and tetrahedron elements into multiple thickness levels, as shown in Fig. 4. While increasing the number of levels may enhance optimization results, it also entails greater computational costs. To strike a balance between optimization efficiency and accuracy, we conducted experiments where we divided the thickness levels into six discrete levels. This ensured a satisfactory level of precision in the optimization process.

During the optimization process, the compliance of all polyhe-

dral elements is sorted from high to low. Subsequently, the thickness of certain polyhedral elements is adjusted accordingly. This iterative process continues until the objective function converges, resulting in a well-distributed internal material arrangement within the model and a stable volume ratio. To initialize the volume fraction value of all polyhedral elements, a value of 1 is assigned. The thickening ratio and thinning ratio of each element are then determined based on the target volume fraction and the current model volume fraction. These ratios indicate the rate at which the wall thickness of each polyhedral element will be increased or decreased in each iteration. The optimization process is based on the Bidirectional Evolutionary Structural Optimization (BESO) method [HX08], which provides stable solutions for the thickening ratio (p_{add}) and thinning ratio (p_{dec}) of each polyhedral element. We classify the cases of V_{target} and V_{now} into five categories, each associated with a specific calculation method to determine the values of p_{add} and p_{dec}, as shown in Table 1,

Cases	p_{add}	p_{dec}
$\frac{V_{now}}{V_{all}} \leq \frac{V_{target}}{V_{all}} - 5\%$	$\frac{V_{target} - V_{now}}{V_{all}}$	$\frac{p_{add}}{2}$
$\frac{V_{target}}{V_{all}} - 5\% < \frac{V_{now}}{V_{all}} < \frac{V_{target}}{V_{all}}$	5%	2.5%
$\frac{V_{now}}{V_{all}} \approx \frac{V_{target}}{V_{all}}$	2.5%	2.5%
$\frac{V_{target}}{V_{all}} < \frac{V_{now}}{V_{all}} < \frac{V_{target}}{V_{all}} + 5\%$	2.5%	5%
$\frac{V_{now}}{V_{all}} \geq \frac{V_{target}}{V_{all}} + 5\%$	$\frac{p_{dec}}{2}$	$\frac{V_{target} - V_{now}}{V_{all}}$

Table 1: *Calculation of p_{add} and p_{dec}*

In instances where the difference between V_{target} and V_{now} is substantial, we dynamically adjust the values of p_{add} and p_{dec} based on this difference to minimize the number of iterations required. Conversely, when the difference between V_{target} and V_{now} is negligible, maintaining optimization accuracy necessitates setting stable and small values for p_{add} and p_{dec}. If V_{target} and V_{now} are similar, it indicates that the current volume ratio has reached the desired target value. Therefore, during the iteration process, it is essential to avoid further changes in the volume ratio by setting p_{add} and p_{dec} to the same value. This helps maintain the stability of the optimization process.
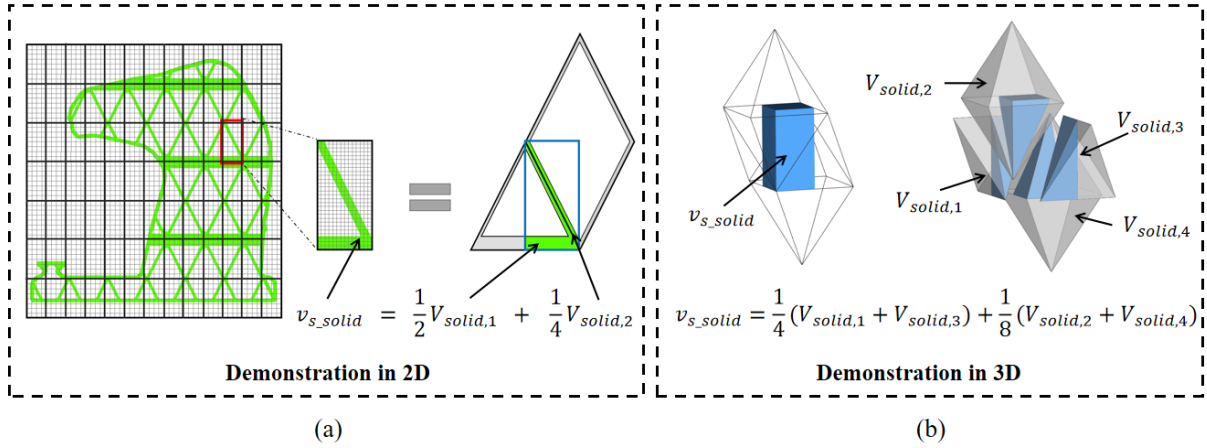
Figure 5: *Illustration of efficient multi-scale finite element calculation. (a) The design domain is discretized with super elements and background elements, and the structure of a single super element is displayed in detail. (b) A 3D demonstration shows the fitting and volume relationship between the periodic polyhedron elements and the elements in finite element calculation.*

4.3. Fast finite element calculation

Efficiency in finite element analysis is crucial for determining the overall efficiency of the optimization algorithm, particularly when fine structure optimization utilizing the finite element method is involved. Such optimization often demands high mesh density, resulting in significant computational burdens that strain computing resources and prolong the optimization process. To address this challenge, we integrate the finite element method with the polyhedron element structure. This integration reduces the mesh density requirement, thereby alleviating the computational burden associated with the optimization task.

Earlier research, as cited in references [NPSL10, WZZD22, HWL*20], has employed a multi-scale methodology to reduce computational costs. This approach strikes a balance between calculation efficiency and accuracy by dividing the model into regular hexahedral elements known as super elements, which are further subdivided into smaller regular hexahedral elements called background elements, as shown in Fig 5 (a). The coarse finite elements (super elements) are utilized to interpolate the displacement field, while the refined background finite elements (background elements) capture the high-resolution structural geometry. By representing the model using super and background elements, the stiffness matrix of the i-th super element can be expressed as follows:

$$K_i = \int_{\Omega_i} B^T D_i B dV \approx \sum_{j=1}^{n_b} E_{ij} B(r_{ij})^T D_0 B(r_{ij}) v_b, \quad (11)$$

where Ω_i is the region of the i-th super element, B is the strain matrix, D_i is the constitutive matrix, n_b is the number of background elements in a super element, D_0 corresponds to the constitutive matrix of the solid material with unit Young's modulus, r_{ij} is the the coordinate of the j-th background element in i-th super element, v_b is the volume of the background element, and E_{ij} is the Young's modulus of the j-th background element in the i-th super element.

K_i can be expressed using the alternative material model [Ben89]

as:

$$\begin{cases} K_i = \sum_{j=1}^{n_b} \frac{1}{8} \sum_{l=1}^{8} (H(\phi_{ijl}))^q K_0, \\ H(\phi_{ijl}) = 1, \quad if \quad \phi_{ijl} \in solid, \\ H(\phi_{ijl}) = 0, \quad if \quad \phi_{ijl} \in empty, \end{cases} \quad (12)$$

where K_0 is the stiffness matrix of the background element in initial case, ϕ_{ijl} represents the coordinate of the l-th vertex on the j-th background element in the i-th super element, and q is the penalty coefficient, which is set to 2 by default.

By taking into account the case of infinitely subdividing the background elements while keeping the super elements unchanged, we can refine the previous formula. As the number of background elements within each super element approaches infinity, the size of each background element tends to zero. Consequently, the coordinates of the eight points on each background element ϕ_{ijl} converge towards the center coordinates ϕ_{ij_center} of the background element

$$\begin{cases} K_i = \sum_{j=1}^{\infty} (H(\phi_{ij\_center}))^q K_0, \\ H(\phi_{ij\_center}) = 1, \quad if \phi_{ij\_center} \in solid, \\ H(\phi_{ij\_cnter}) = 0, \quad if \phi_{ij\_center} \in empty. \end{cases} \quad (13)$$

Taking into account the straightforward geometry of our self-supporting infill structure, resulting in a nearly consistent material distribution within each solid component, it follows that when the discretized super elements and background elements are adequately diminutive, we can recast the aforementioned formula in relation to volume fraction in the subsequent manner:

$$K_i \approx \frac{v_{s\_solid}}{v_{s\_whole}} K_0, \quad (14)$$

where v_{s_solid} is the volume of the entity structure in the super element and v_{s_whole} denotes the total volume of the super element, as depicted in Fig 5. By using a coarser mesh, we can easily calculate

v_{s_solid} and v_{s_whole}, and thus represent the fine structure. Hence, we combine the periodic polyhedron element structure with the super element finite element grids, resulting in:

$$K_i = a_i \sum_{j=1}^{4} b_{ij} \frac{V_{solid,j}}{V_{polyhedron,j}} K_0, \qquad (15)$$

where a_i denotes the proportion of the initial model in the i-th super element ($0 \leq a_i \leq 1$), b_{ij} is the proportion of the j-th polyhedron element in the i-th super element. For octahedral polyhedron elements, b_{ij} is equal to $\frac{1}{3}$, while for tetrahedral polyhedron elements, it is $\frac{1}{6}$. Moreover, $\frac{V_{solid,j}}{V_{polyhedron,j}}$ represents the volume fraction of the polyhedron element. By aligning the periodic polyhedron element structure with the super element, we can readily determine the values of a_i and b_{ij}. This enables us to employ a coarser mesh to represent the fine structure, leading to significant improvements in computational efficiency.

To calculate the compliance of each polyhedral polyhedron element, we employ a local homogenization method. In this approach, the polyhedron element is formed by combining portions of multiple hexahedral elements. Therefore, we only require the compliance values of the hexahedral elements that make up the polyhedron element. By summing these compliance values, we can determine the compliance of the polyhedral polyhedron element, denoted as C_j. Specifically, we assume that the compliance values of all background elements within the super element are uniform. Hence, we obtain C_j by summing these compliance values

$$C_j = \sum_{i=1}^{k} C_{ij} = \sum_{i=1}^{k} b_{ij} c_{ij}, \qquad (16)$$

where C_{ij} denotes the partial compliance contributed by the i-th super element that forms the j-th polyhedron element, while c_{ij} is the compliance of the i-th super element within the j-th polyhedron element.

The horse head model is optimized in our study by applying a pressure load on its top surface and fixing the bottom surface, as depicted in Fig 6. Throughout the optimization process, the volume fraction continuously decreases. As the volume approaches the target volume, the rate of volume reduction gradually slows down. Our method employs an accelerated volume reduction strategy in the early stages of optimization to reduce the number of iterations. In the later stages, when precise adjustments to the model's structure are required, the algorithm slows down the rate of volume reduction to ensure the accuracy of the optimized result. This approach ensures a steady convergence towards meeting the design requirements, as observed in the overall trend of the optimization process.

4.4. Topology Optimization

As some polyhedron elements may have a volume fraction close to zero, corresponding to a very small wall-thickness. These polyhedron elements should be removed or merged, which can be treated as topology optimization. To guarantee manufacturability, a minimum wall thickness T_{min} is imposed on the structure based on the capabilities of the 3D printers. Since each wall in the structure is formed by the combination of walls from two adjacent polyhedron

elements, the relationship between the minimum volume fraction X_{min} of polyhedron elements and the minimum wall-thickness t_{min} of the polyhedron elements can be expressed as

$$t \geq t_{min} = \frac{1}{2} T_{min}, \qquad (17)$$

$$X \geq X_{min} = \frac{V_{solid}}{V_{polyhedron}} = 1 - \left(\frac{w - t_{min}}{w}\right)^3. \qquad (18)$$

It is evident that the volume fraction of the polyhedron element reaches its minimum value, X_{min}, when the wall thickness equals t_{min}. During the topology optimization process, polyhedron elements with a volume fraction below X_{min} are merged by combining small polyhedron elements into a larger polyhedron element. Figure 7 illustrates this process using a two-dimensional rhombus for visualization purposes.

5. Experimental Results and Discussions

To demonstrate the effectiveness of our algorithm, we conducted stiffness optimization experiments on models of different complexities and compared the results with relevant methods. The experiments were carried out on a standard desktop PC equipped with an Intel-i7-9700K 3.6 GHz CPU and 32 GB RAM. Furthermore, we fabricated some of the optimized models using a FDM based 3D printer. For these experiments, we set the initial axial lengths of the polyhedron elements to 2 mm and 4 mm for the two dimensions w and h, respectively. The number of initial elements is related to the complexity of 3D models and the required precision. While augmenting the element count would improve accuracy, it would also elevate computational intricacy

5.1. The effect of polyhedron elements

To investigate the influence of the aspect ratio $\frac{h}{w}$ of the polyhedron elements on the optimization results, we conducted an experiment where we varied the aspect ratio while keeping other conditions constant. In Fig 8, we compared the optimization results by performing mechanical experiments with aspect ratios of $\frac{h}{w} = 1.5$, $\frac{h}{w} = 2$, and $\frac{h}{w} = 2.5$. All the models were subjected to a top pressure of 0.9 MPa with the bottom fixed. The maximum Mises stress values for the three models were 1.92 MPa, 2 MPa, and 1.97 MPa, respectively. The stress diagrams indicate that the aspect ratio $\frac{h}{w}$ has a minimal effect on the optimization results due to the involvement of the optimization algorithm. The stress concentration areas in all three models are located at the bottom of the right side of the root, which has been optimized into a solid body, yielding a similar mechanical effect. However, considering the practicality of different printing equipment and materials, we chose an aspect ratio of $\frac{h}{w} = 2$.

5.2. The effect of discrete thickness levels

To assess the impact of discrete thickness levels on our optimization, we performed an optimization study on the molar model using different thickness levels: 3, 6, 11, and 51. Figure 9 presents the mechanical analysis results of the optimized models with varying thickness levels (3, 6, 11, and 51) under the same volume fraction of 50%, with identical external loads, constraint conditions,
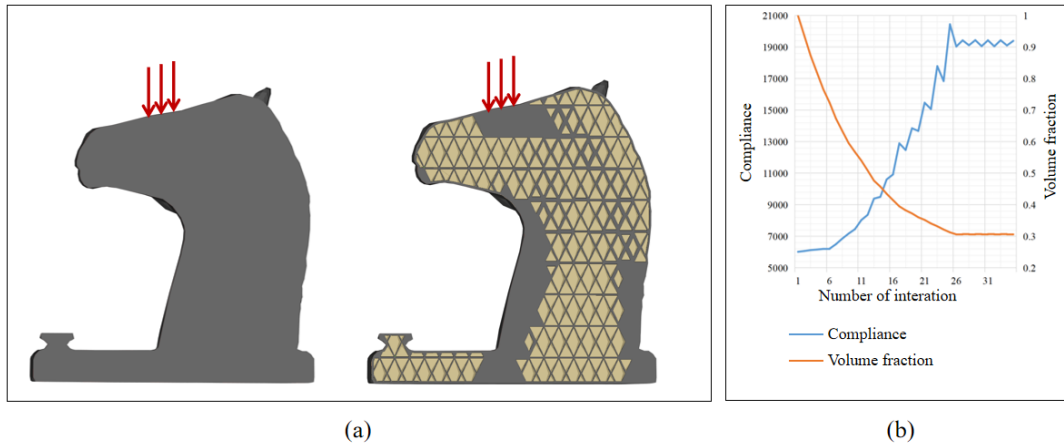
Figure 6: *Illustration of the thickness optimization. (a) The models before and after optimization under a top load. (b) The convergence curves of model compliance and volume fraction during the optimization process.*

Table 2: *Model optimization time (second) and volume fraction.*

|	Preprocess (s)	Optimization			Postprocess (s)	Total Time (s)	Element number	Result Volume	Volume Fraction
		Iteration	Time (s)	Total Time (s)					
Bunny	36.9	28	8.56	239.6	63	339.5	37800	55714.75	43.3%
Kitten	16.9	31	7.3	226.9	28.5	272.3	32340	68746	52.6%
Horse head	16.6	35	2.47	86.4	51.6	154.6	18900	27976.2	47.3%
Molar(rate=1.5)	444	30	6.65	199.7	925.6	1569.3	21762	50129.1	44%
Molar(rate=2)	14.17	30	3.85	115.4	31	160.6	23436	50317.5	44.2%
Molar(rate=2.5)	14.13	33	2.28	75.36	30.2	119.7	18414	50775.3	44.6%
Shark (3 levels)	21.6	15	12.4	185.2	31.4	238.2	44550	33398.1	50.4%
Shark (6 levels)	21.3	27	13.15	354.9	30.9	407.1	44550	33023	50%
Shark (11 levels)	21.2	51	12.98	662.2	31.1	714.5	44550	33025.4	50%
Shark (51 levels)	20.9	224	13.1	2932.3	30.6	2983.8	44550	33142.9	50%
Unicorn	51.6	36	2.58	93.7	111	256.3	13662	12389.8	63.4%
Elephant	44.9	34	5	173	146.6	364.6	31185	49380.2	46.9%
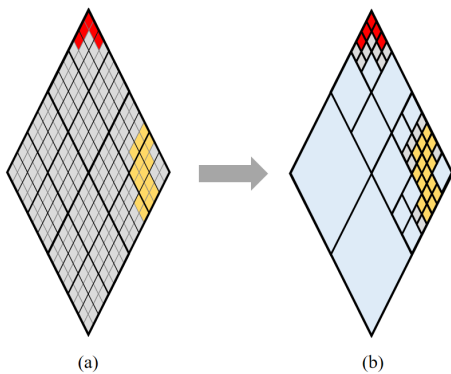
Figure 7: *Illustration of topology optimization in 2D. The red rhombuses denote the polyhedron element providing support for the overhang part of the model shell. The yellow rhombuses represent the polyhedron elements with large volume fraction after stiffness optimization, while the gray parts indicate the polyhedron element with a volume fraction near zero. (b) illustrates the polyhedron element structure after element merging in topology optimization.*

and material parameters. The corresponding Mises stress values are 6.93 MPa, 4.0 MPa, 3.847 MPa, and 3.909 MPa, respectively. It is evident that the optimization result with six thickness levels differs significantly from the other three results. Notably, the maximum Mises stress value is considerably larger than that of the other groups. However, there is no notable difference in the structural and simulation results among the other three groups.

Furthermore, we compared the optimization times among the four groups. When using 3 thickness levels, it required 15 iterations and 185.2 seconds to complete the thickness optimization process. With 6 thickness levels, it took 29 iterations and 372.3 seconds. For 11 thickness levels, it required 51 iterations and 662.2 seconds. Finally, with 51 thickness levels, it took 224 iterations and 2932.3 seconds for the thickness optimization. As the density of thickness levels increases, more iterations are needed for optimization, while the time per iteration remains constant. This leads to a significant increase in the total time required for thickness optimization. However, if the density of thickness levels becomes too high, it does not have a significant positive impact on the final optimization result but significantly reduces the efficiency of the algorithm. Consid-
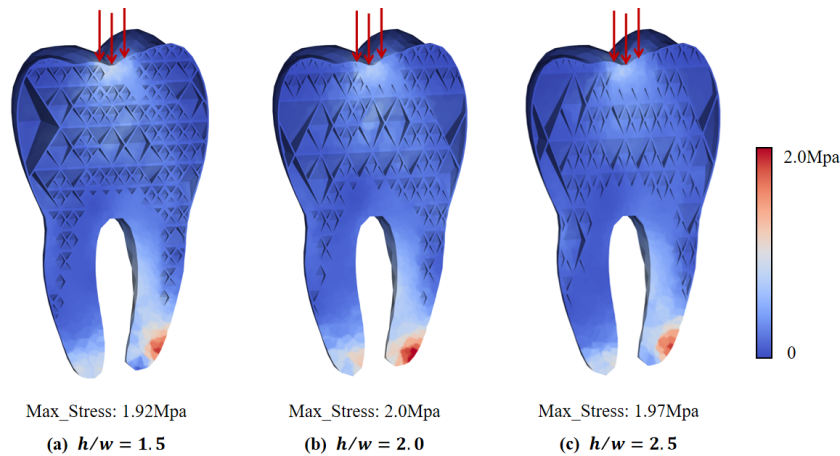
Max_Stress: 1.92Mpa	Max_Stress: 2.0Mpa	Max_Stress: 1.97Mpa
(a) $h/w = 1.5$	**(b)** $h/w = 2.0$	**(c)** $h/w = 2.5$

Figure 8: *Effect of the aspect ratio $\frac{h}{w}$. The molar model is processed with a volume fraction of 44%, and the optimization results of the aspect ratio parameters $\frac{h}{w}$ with 1.5, 2, and 2.5 are compared for mechanical analysis.*
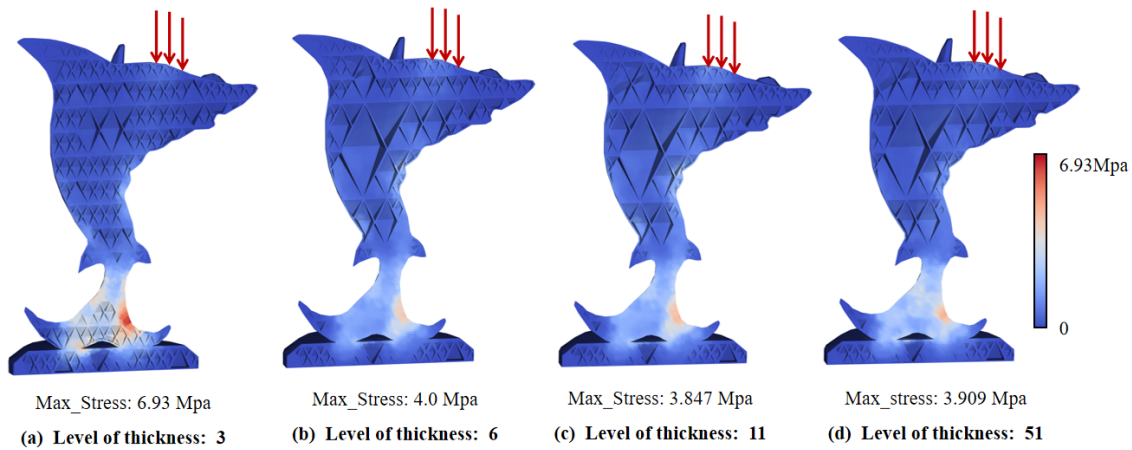

Max_Stress: 6.93 Mpa	Max_Stress: 4.0 Mpa	Max_Stress: 3.847 Mpa	Max_stress: 3.909 Mpa
(a) Level of thickness: 3	**(b) Level of thickness: 6**	**(c) Level of thickness: 11**	**(d) Level of thickness: 51**

Figure 9: *Effect of discrete thickness levels. The mechanical analysis results of optimized sharks with different thickness dispersion levels (3, 6, 11, and 51) under the same volume fraction of 50% with the same loading.*

ering these factors, we have selected six levels of thickness as the default option.

5.3. Comparing with other structures

To evaluate the effectiveness of our algorithm, we conducted a comparison between our optimized structures and other relevant structures under identical conditions, including volume fraction, loading, and material properties. In Figure 10, we compared our optimized structure with two other self-supporting structures from different studies. The first structure, optimized in [WWZW16], achieved a volume ratio of 54%. The second structure, from [XLY*21], is not optimized due to its algorithm limitations. Both structures were subjected to the same external load, restraint conditions, and material parameters as our optimized structure, using the kitten model. Our optimized structure demonstrated a maximum stress of 1.2 MPa, which is significantly lower

than the maximum stresses of 3.35 MPa in [WWZW16] and 2.12 MPa in [XLY*21]. These results indicate that our structure exhibits superior mechanical performance compared to the other two self-supporting structures. Moreover, by conserving a substantial amount of material in these non-stress-concentrated regions, our algorithm gains higher optimization flexibility. As a result, even when maintaining the same overall volume ratio, our optimization approach achieves superior results in terms of mechanical performance.

In Figure 11, we present a comparison of the mechanical performance between our optimized method and two other optimized non-self-supporting structures. The comparison is conducted using the shark model with a volume fraction of 44%, while maintaining the same external load, constraint conditions, and material parameters. Our method demonstrates superior mechanical performance, as indicated by the maximum stress value of 2.6 MPa. This value is
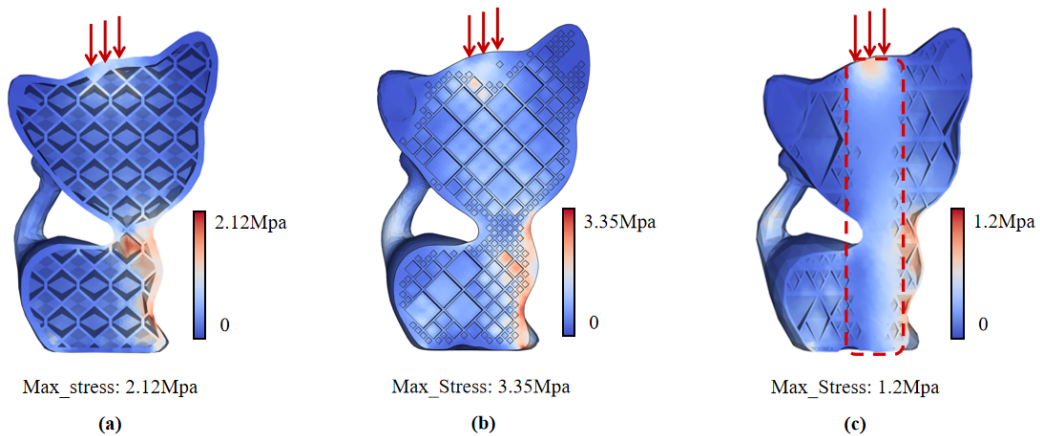
Figure 10: *Comparison with other self-supporting structures. Our structure (c) has better mechanical performance than the structure in [WWZW16] (b) and Structure in [XLY*21] (a) with a volume ratio of 54%.*
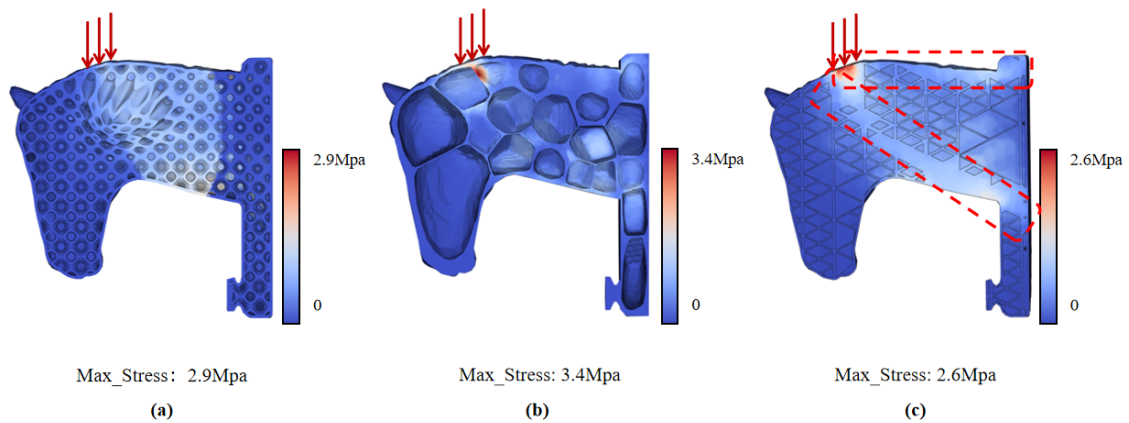

Figure 11: *Comparison with non-self-supporting structures. Our structure achieves a maximum stress of 2.6 MPa, which is significantly lower than the maximum stress of 2.9 MPa for [HWL*20] (a) and 3.4 MPa for [LSZ*14] (b) with a volume ratio of 44%.*

significantly lower than the maximum stresses obtained by the non-self-supporting structures in [HWL*20] (2.9 MPa) and [LSZ*14] (3.4 MPa). These results highlight the effectiveness of our optimization approach in achieving enhanced structural strength and load-bearing capabilities compared to the alternative methods.

Furthermore, we conducted a comparison between the mechanical performance of structures before and after optimization, with volume ratios of 47.3% (horse head) and 54.5% (kitten). The initial structures before optimization are depicted in Figures 12 (a) and (c), while the optimized structures are shown in Figures 12 (b) and (d). This comparison highlights the effectiveness of our optimization approach in enhancing the mechanical performance of the structures. The optimized structures exhibit lower maximum Mises stress and a more uniform distribution of stress throughout the models. This improvement in mechanical performance is evident, as the optimized structures are better able to withstand external loads and maintain structural integrity.

5.4. More results

We recorded the time information and the volume fraction in optimization process in Table 2. The results show that our algorithm can effectively optimize the stiffness and reduce the weight of the model while ensuring good performance efficiency. To demonstrate the applicability of our method, more optimized results are illustrated in Fig. 13. We selected models which are also manufactured using FDM based 3D printing, as shown in Fig. 14. The printed model has a maximum length of around 20cm, while the smallest octahedral unit has a width of 4mm.

5.5. Limitation and future work

In this method, we improve the algorithm's efficiency by establishing a mapping relationship between finite element elements and polyhedral elements. However, the current mapping approach is based on segmenting and combining the flexibility values, which limits the diversity of the resulting polyhedral structures.
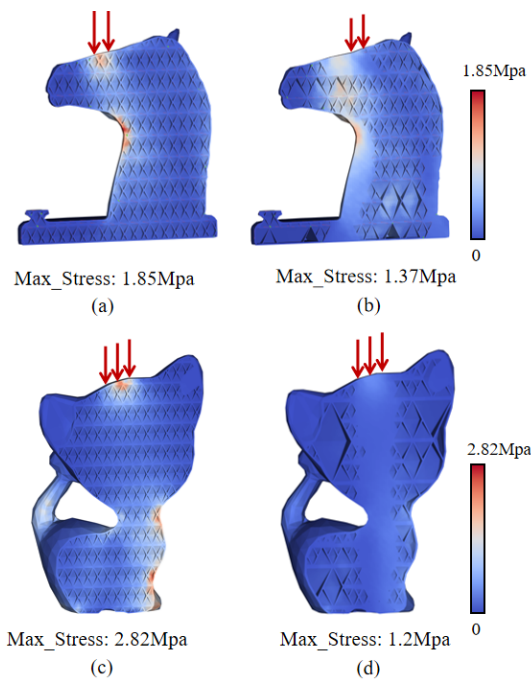
Figure 12: *Comparison of structures before and after optimization with volume ratios of 47.3% (horse head) and 54.5% (kitten). (a) and (c) The initial structures before optimization. (b) and (d) The optimized structures.*

In future research, we aim to explore a more diverse range of structures that can be efficiently calculated. By expanding the shape possibilities of polyhedral elements and exploring alternative mapping strategies, we can further enhance the algorithm's capabilities and enable it to optimize a wider variety of structures in a fast and efficient manner.

6. Conclusions

In this paper, we propose a novel approach to represent and optimize a self-supporting structure. Compared to existing self-supporting structure optimization methods, our approach incorporates adaptive improvements to the finite element calculation to enhance the algorithm's efficiency. The resulting structure is a highly robust, porous, and self-supporting surface. Our algorithm excels in both computational efficiency and stiffness, and the optimized models can be 3D printed without the need for any additional internal support. Various experimental results demonstrate the effectiveness and robustness of our method.
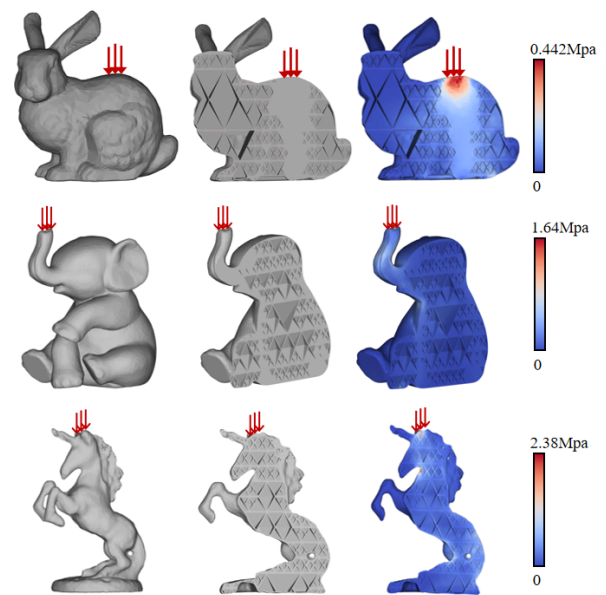
Acknowledgement

Figure 13: *More results, including Bunny, Elephant and Unicorn with volume fraction of 43.3%, 46.9% and 63.4%, respectively.*

References

[BAH11] BRACKETT D., ASHCROFT I., HAGUE R.: Topology optimization for additive manufacturing. In *Solid Freeform Fabrication Proceedings* (Austin, TX(US), 2011), Wofson Schoo of Mechnic nd Mnufcuring Engineering, Loughborough Universiy, Loughborough, Leicesershire, LE11 3TU, UK, pp. 348–362. 2

[Ben89] BENDSØE M. P.: Optimal shape design as a material distribution problem. *Structural optimization 1* (1989), 193–202. 3, 6

[BK88] BENDSØE M. P., KIKUCHI N.: Generating optimal topologies in structural design using a homogenization method. *Applied Mechanics and Engineering 71* (1988), 197–224. 3

[BTX20] BI M., TRAN P., XIE Y. M.: Topology optimization of 3d continuum structures under geometric self-supporting constraint. *Additive Manufacturing 36* (2020), 101422. 3

[GG16] GAYNOR A. T., GUEST J. K.: Topology optimization considering overhang constraints: Eliminating sacrificial support material in additive manufacturing through design. *Structural & Multidisciplinary Optimization 54*, 5 (2016), 1157–1172. 2

[GZR*15] GAO W., ZHANG Y., RAMANUJAN D., RAMANI K., CHEN Y., WILLIAMS C. B., WANG C. C. L., SHIN Y. C., ZHANG S., ZAVATTIERI P. D.: The status, challenges, and future of additive manufacturing in engineering. *Comput. Aided Des. 69* (2015), 65–89. 2

[GZZ14] GUO X., ZHANG W., ZHONG W.: Doing topology optimization explicitly and geometrically—a new moving morphable components based framework. *Journal of Applied Mechanics 81* (2014), 081009. 3

[HWL*20] HU J., WANG S., LI B., LI F., LUO Z., LIU L.: Efficient representation and optimization for tpms-based porous structures. *IEEE Transactions on Visualization and Computer Graphics* (2020), 1–1. 2, 6, 10

[HX08] HUANG X., XIE Y. M.: Bi-directional evolutionary topology optimization of continuum structures with one or multiple materials. *Computational Mechanics 43* (2008), 393–401. 3, 5

[KWW19] KUIPERS T., WU J., WANG C. C. L.: Crossfill: Foam structures with graded density for continuous material extrusion. *Comput. Aided Des. 114* (2019), 37–50. 1, 2
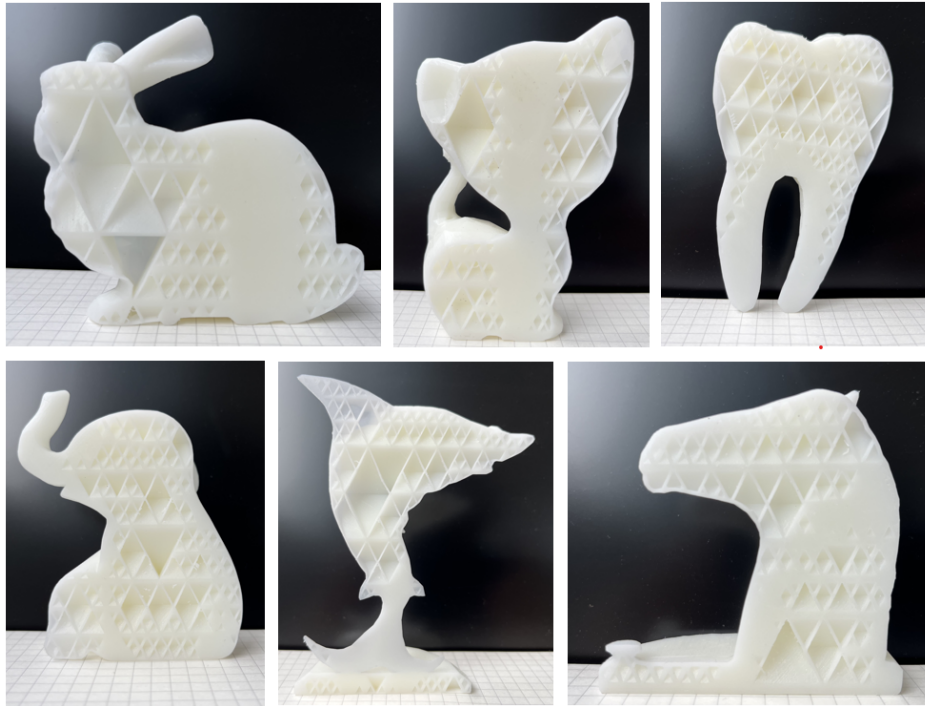
Figure 14: *3D printed models.*

[LBRM12] LUO L., BARAN I., RUSINKIEWICZ S., MATUSIK W.: Chopper: Partitioning models into 3d-printable parts. *ACM Transactions on Graphics (TOG) 31*, 6 (2012), 1–9. 2

[LFR*18] LEE M., FANG Q., RYU J., LIU L., KIM D.-S.: Support-free hollowing for 3d printing via voronoi diagram of ellipses. *ArXiv abs/1708.06577* (2018). 1, 3

[LGC*18] LIU J., GAYNOR A. T., CHEN S., KANG Z., SURESH K., TAKEZAWA A., LI L., KATO J., TANG J., WANG C. C., CHENG L., LIANG X., TO A. C.: Current and future trends in topology optimization for additive manufacturing. *Struct. Multidiscip. Optim. 57*, 6 (jun 2018), 2457–2483. 2

[LMT*14] LEARY M., MERLI L., TORTI F., MAZUR M., BRANDT M.: Optimal topology for additive manufacture: A method for enabling additive manufacture of support-free optimal structures. *Materials & Design 63* (2014), 678–690. 2

[LSLL20] LUO Y., SIGMUND O., LI Q., LIU S.: Additive manufacturing oriented topology optimization of structures with self-supported enclosed voids. *Computer Methods in Applied Mechanics and Engineering 372* (2020), 113385. 2

[LSWW14] LIU L., SHAMIR A., WANG C. C. L., WHITING E.: 3d printing oriented design: geometry and optimization. *SIGGRAPH Asia 2014 Courses* (2014). 2

[LSZ*14] LU L., SHARF A., ZHAO H., WEI Y., FAN Q., CHEN X., SAVOYE Y., TU C., COHEN-OR D., CHEN B.: Build-to-last: Strength to weight 3d printed objects. *Acm Transactions on Graphics 33*, 4 (jul 2014). doi:10.1145/2601097.2601168. 1, 2, 10

[MHSL18] MARTÍNEZ J., HORNUS S., SONG H.-C., LEFEBVRE S.: Polyhedral voronoi diagrams for additive manufacturing. *ACM Transactions on Graphics (TOG) 37* (2018), 1 – 15. 1, 2

[NPSL10] NGUYEN T. H., PAULINO G. H., SONG J., LE C. H.: A computational paradigm for multiresolution topology optimization (MTOP). *Structural and Multidisciplinary Optimization 41*, 4 (2010), 525–539. 6

[PAHA18] PANESAR A., ABDI M., HICKMAN D., ASHCROFT I. A.: Strategies for functionally graded lattice structures derived using topology optimisation for additive manufacturing. *Additive manufacturing 19* (2018), 81–94. 3

[PP19] PLOCHER J., PANESAR A.: Review on design and structural optimisation in additive manufacturing: Towards next-generation lightweight structures. *Materials & Design 183* (2019), 108164. 1

[RL16] REINER T., LEFEBVRE S.: Interactive modeling of support-free shapes for fabrication. In *Proceedings of the 37th Annual Conference of the European Association for Computer Graphics: Short Papers* (Goslar, DEU, 2016), EG '16, Eurographics Association, p. 25–28. 2

[Roz01] ROZVANY G. I. N.: Aims, scope, methods, history and unified terminology of computer-aided topology optimization in structural mechanics. *Structural and Multidisciplinary Optimization 21* (2001), 90–108. 3

[SK91] SUZUKI K., KIKUCHI N.: A homogenization method for shape and topology optimization. *Computer Methods in Applied Mechanics and Engineering 93* (1991), 291–318. 3

[SM13] SIGMUND O., MAUTE K.: Topology optimization approaches. *Structural and Multidisciplinary Optimization 48* (2013), 1031–1055. 3

[SMREC15] SÁ A. M., MELLO V. M., RODRIGUEZ-ECHAVARRIA K., COVILL D.: Adaptive voids. *The Visual Computer 31* (2015), 799–808. 2

[SVB*12] STAVA O., VANEK J., BENES B., CARR N., MĚCH R.: Stress relief: improving structural strength of 3d printable objects. *ACM Transactions on Graphics (TOG) 31*, 4 (2012), 1–11. 2

[SW00] SETHIAN J. A., WIEGMANN A.: Structural boundary design via level set and immersed interface methods. *Journal of Computational Physics 163* (2000), 489–528. 3

[TKF15] TANGYUNLONG, KURTZAIDAN, FIONA Z.: Bidirectional evolutionary structural optimization (beso) based design method for lat-

tice structure to be fabricated by additive manufacturing. *Computer-aided Design* (2015). 3

[VGB14a] VANEK J., GALICIA J. A. G., BENES B.: Clever support: Efficient support structure generation for digital fabrication. In *Computer graphics forum* (2014), vol. 33, Wiley Online Library, pp. 117–125. 2

[VGB*14b] VANEK J., GALICIA J. G., BENES B., MĚCH R., CARR N., STAVA O., MILLER G.: Packmerger: A 3d print volume optimizer. In *Computer Graphics Forum* (2014), vol. 33, Wiley Online Library, pp. 322–332. 2

[WAWS18] WU J., AAGE N., WESTERMANN R., SIGMUND O.: Infill optimization for additive manufacturing—approaching bone-like porous structures. *IEEE Transactions on Visualization and Computer Graphics 24* (2018), 1127–1140. 2

[WLW*18] WANG W. M., LIU Y.-J., WU J., TIAN S., WANG C. C. L., LIU L., LIU X.: Support-free hollowing. *IEEE Transactions on Visualization and Computer Graphics 24* (2018), 2787–2798. 3

[WM17] WALTON D., MOZTARZADEH H.: Design and development of an additive manufactured component by topology optimisation. *Procedia CIRP 60* (2017), 205–210. 3

[WQL*17] WANG W. M., QIAN S. Z., LIN L., LI B., YIN B., LIU L., LIU X.: Support-free frame structures. *Comput. Graph. 66* (2017), 154–161. 1, 3

[WWmG03] WANG M. Y., WANG X., MING GUO D.: A level set method for structural topology optimization. *Computer Methods in Applied Mechanics and Engineering 192* (2003), 227–246. 3

[WWY*13] WANG W., WANG T. Y., YANG Z., LIU L., TONG X., TONG W., DENG J., CHEN F., LIU X.: Cost-effective printing of 3d objects with skin-frame structures. *ACM Trans. Graph. 32*, 6 (nov 2013). 1, 2

[WWZW16] WU J., WANG C. C. L., ZHANG X., WESTERMANN R.: Self-supporting rhombic infill structures for additive manufacturing. *Comput. Aided Des. 80* (2016), 32–42. 1, 2, 4, 9, 10

[WZZD22] WANG Y., ZHENG W., ZHENG Y., DA D.: A new three-level mesh method to accelerate the structural topology optimization. *Applied Mathematical Modelling 109* (2022), 374–400. 6

[XC17] XIE Y., CHEN X.: Support-free interior carving for 3d printing. *Vis. Informatics 1* (2017), 9–15. 3

[XLY*21] XU W., LIU Y., YU M. S., WANG D.-X., HOU S., LI B., WANG W. M., LIU L.: A support-free infill structure based on layer construction for 3d printing. *IEEE transactions on visualization and computer graphics PP* (2021). 1, 9, 10

[XS93] XIE Y. M., STEVEN G. P.: A simple evolutionary procedure for structural optimization. *Computers & Structures 49* (1993), 885–896. 3

[YCF18] YANG Y., CHAI S., FU X.-M.: Computing interior support-free structure via hollow-to-fill construction. *Comput. Graph. 70* (2018), 148–156. 3

[ZNLC14] ZAVALA G. R., NEBRO A. J., LUNA F., COELLO C. A. C.: A survey of multi-objective metaheuristics applied to structural optimization. *Structural and Multidisciplinary Optimization 49* (2014), 537–558. 3

[ZR91] ZHOU M., ROZVANY G. I. N.: The coc algorithm, part ii: Topological, geometrical and generalized shape optimization. *Computer Methods in Applied Mechanics and Engineering 89* (1991), 309–336. 3

[ZSZ21] ZHOU L., SIGMUND O., ZHANG W.: Self-supporting structure design with feature-driven optimization approach for additive manufacturing. *Computer Methods in Applied Mechanics and Engineering 386* (2021), 114110. 2

[ZWL*22] ZHANG L., WANG S., LI B., WANG Y., LUO Z., LIU L.: Function representation based analytic shape hollowing optimization. *Computer-Aided Design 144* (2022), 103156. 2

[ZXW*15] ZHANG X., XIA Y., WANG J., YANG Z., TU C., WANG W.: Medial axis tree - an internal supporting structure for 3d printing. *Comput. Aided Geom. Des. 35-36* (2015), 149–162. 1, 2

[ZYZ*17] ZHANG W., YANG W., ZHOU J., LI D., GUO X.: Structural topology optimization through explicit boundary evolution. *Journal of Applied Mechanics 84* (2017), 011011. 3

[ZZG16] ZHANG W., ZHU J., GAO T.: 7 - potential applications of topology optimization. In *Topology Optimization in Engineering Structure Design*, Zhang W., Zhu J., Gao T., (Eds.). Elsevier, 2016, pp. 239–250. 3

[ZZW*21] ZHU J., ZHOU H., WANG C., ZHOU L., YUAN S., ZHANG W.: A review of topology optimization for additive manufacturing:status and challenges. *Chinese Journal of Aeronautics 34*, 1 (2021), 20. 2